Hydrodynamic optimization of ship hull forms

Article *in* Applied Ocean Research · December 2001

DOI: 10.1016/S0141-1187(02)00002-0

3 authors, including:

Dane Hendrix
Naval Surface Warfare Center, Carderock, U…
17 PUBLICATIONS **154** CITATIONS
SEE PROFILE

Francis Noblesse
Shanghai Jiao Tong University
106 PUBLICATIONS **736** CITATIONS
SEE PROFILE

ELSEVIER

Applied Ocean Research 23 (2001) 337–355

Applied Ocean Research

www.elsevier.com/locate/apor

Hydrodynamic optimization of ship hull forms

Scott Percival, Dane Hendrix, Francis Noblesse*

David Taylor Model Basin, NSWC-CD 9500 MacArthur Blvd, West Bethesda, MD 20817-5700, USA

Received 25 June 2001; revised 21 November 2001; accepted 26 November 2001

Abstract

An extremely simple CFD tool is used to compare the calm-water drags of a series of hull forms and to define 'optimized' monohull ships for which the total (friction + wave) calm-water drag is minimized. The friction drag is estimated using the classical ITTC formula. The wave drag is predicted using the zeroth-order slender-ship approximation. Comparisons of theoretical predictions and experimental measurements for a series of eight hull forms show that—despite the extreme simplicity of the method that is used here to estimate the friction drag and the wave drag—the method is able to rank the drags of a series of hull forms roughly in accordance with experimental measurements. Thus, the method may be used, with appropriate caution, as a practical hull form design and optimization tool. For purposes of illustration, optimized hull forms that have the same displacement and waterplane transverse moment of inertia as the classical Wigley hull, taken as initial hull in the optimization process, are determined for three speeds and for a speed range. © 2002 Published by Elsevier Science Ltd.

Keywords: Optimization; Hull forms; Calm-water

1. Introduction

Although CFD-based hull form optimization is not routinely used for ship design, a significant number of applications of CFD tools to hydrodynamic optimization—mostly for reducing calm-water drag and wave patterns—attest to a growing interest in hydrodynamic optimization. This growing interest in hydrodynamic optimization is a useful development because—in principle—ship design implies optimization, e.g. minimization of a functional that appropriately weighs payload, ship speed, motions, and calm-water drag.

Optimization of a ship hull form involves a number of nontrivial issues, including selection of an appropriate objective function, choice of optimization scheme, geometrical representation of hull surface and choice of related design variables and constraints, selection of a practical and robust CFD tool to evaluate the objective function, and decision to perform optimization for a single-point design or for multiple-point design, e.g. for a single ship speed or for a range of speeds. These basic issues involved in hull form optimization have been addressed in various ways in the literature, and are now briefly considered in turn.

Regarding objective functions, it is well understood that hydrodynamic optimization needs to take into account a number of requirements, including speed, calm-water drag, motions and loads, and other considerations like payload, propulsion, and wakes. In particular, an integrated approach that simultaneously considers motions and calm-water drag should be used because minimization of ship motions without regard to drag, or of drag without regard to seakeeping characteristics, can lead to unacceptable designs. However, the much simpler task of minimizing objective functions associated with calm-water flow features (wave resistance or total drag, and/or wave patterns) is considered in all the CFD applications to hull form optimization that are listed further on, and in the present study as well.

Several optimization algorithms have been used in the literature. Three algorithms (steepest descent, conjugate gradient, sequential quadratic programming) are considered in Ref. [1], and genetic algorithm techniques are used in Refs. [2,3]. A hybrid method based on coupling of a genetic algorithm and a hill-climbing technique is used in Ref. [4]. Alternative ways, noted in Ref. [1], of representing the hull surface modifications that are required in a hull form optimization procedure have been employed.

With regard to CFD tools, both extremely simple tools—Michell's thin-ship approximation and the slender-ship approximation given in Ref. [5]—and more sophisticated tools—potential-flow panel methods based on Rankine

* Corresponding author. Tel.: +1-301-227-7018; fax: +1-301-227-4607.
E-mail address: noblessefl@nswccd.navy.mil (F. Noblesse).

0141-1187/02/$ - see front matter © 2002 Published by Elsevier Science Ltd.
PII: S0141-1187(02)00002-0

sources and RANS-based viscous-flow methods—have been used.

Thin-ship theory is used in Refs. [3,6–12,33]. The hull form optimization results reported in Refs. [13–15], are based on the slender-ship approximation. Ref. [16] relies on the slender-ship approximation and the Fourier–Kochin flow representation given in Refs. [17,18].

A combination of a Rankine-source panel method and simpler prediction tools are used in Ref. [1] to speed up the optimization procedure. Refs. [1,2,9,19–22], use potential-flow panel methods based on Rankine sources. RANS-based viscous-flow methods are used in Refs. [23–26]. A combination of flow solvers based on potential flow, viscous boundary layer, and RANS is used in Ref. [27].

The usefulness of many currently-available CFD tools for routine applications to hydrodynamic optimization is restricted by various factors. In particular, some CFD tools can only be used within a limited range of ship speed and/or wave frequency. Other tools require highly structured discretizations of the ship hull and the free surface (and even the fluid domain), and may indeed fail to provide reliable results unless a discretization that satisfies stringent requirements is used. Lack of versatility (due to limited range of applicability) or robustness, preprocessing discretization requirements that are overly time consuming (and hence too expensive for routine applications), excessive computational requirements, and need for highly-experienced expert users are factors that can seriously restrict the practical usefulness of a CFD tool for routine practical applications to ship hull form design and, especially, optimization.

Thus, an extremely simple CFD tool is used in this study to estimate the total (friction + wave) calm-water drag of a ship. Specifically, the friction drag is evaluated using the ITTC 1957 model-ship correlation line formula. The calm-water wave drag is estimated using the zeroth-order slender-ship approximation given in Refs. [5,18] because the exceptional simplicity of this calculation method (no nearfield-flow calculations are required) renders it ideally suited for optimization (a one-speed wave drag calculation for a ship hull represented by 8000 panels requires less than 1 s on a gigahertz computer).

This method is used to compare the drags of eight hull forms in the series of hull forms analyzed in Refs. [28,29] within the mid-term sealift ship technology development program. Comparisons of theoretical calculations and experimental measurements of drag for this series of eight hull forms show that—despite the extreme simplicity of the method used here to estimate the friction drag and the wave drag—the method is able to rank the drags of the variant hull forms roughly in agreement with experimental measurements. These results—and those reported in Refs. [14–16]—indicate that rough approximations to the friction drag and the wave drag may be used, with appropriate caution, as a practical hull form optimization tool. Indeed, the method is used to determine optimized hull forms that have the same displacement and water-plane transverse moment of inertia as the classical Wigley hull, which is taken as initial hull in the optimization process for purposes of illustration.

The studies previously published in the literature on hydrodynamic optimization of ship hull forms only consider optimization for a single ship speed. The present study presents both hull forms optimized for a single speed (point optimization) and hull forms optimized for several speeds (multi-point optimization). In fact, a main conclusion of the study is that optimization within a speed-range (multi-point optimization) is much preferable to single-speed optimization, which appears to yield highly-tuned optimized hull forms that perform well only within a fairly narrow speed range centered at the optimization speed.

2. A series of eight hull forms

A series of eight hull forms is considered in this study. These hull forms, previously analyzed in Refs. [28,29] within the mid-term sealift ship technology development program, are variants of the baseline hull form that is depicted in Fig. 1 and is identified as DTMB model 5501 in Refs. [28,29]. The other seven hull forms are identical to the baseline hull form shown in Fig. 1 except for the shape of the bow bulb and/or skeg.

The baseline bulb and six bulb variants are shown in Figs. 1 and 2, respectively. The seven bows consist of the (elliptical) baseline bulb shown in Fig. 1, four nabla-type bulbs, a producible bulb (also elliptical), and a no-bulb bow. The baseline skeg and a producible skeg variant are depicted in Fig. 3.

The series of eight hulls that is considered in this study are identical except for the shapes of the bow bulb and/or skeg. The series consists of the following bulb and skeg combinations:

BULB	SKEG
baseline	baseline
no bulb	baseline
nabla 1	baseline
nabla 2	baseline
nabla 3	baseline
producible	baseline
baseline	producible
nabla 6	producible

These eight bulb/skeg combinations are compared in six

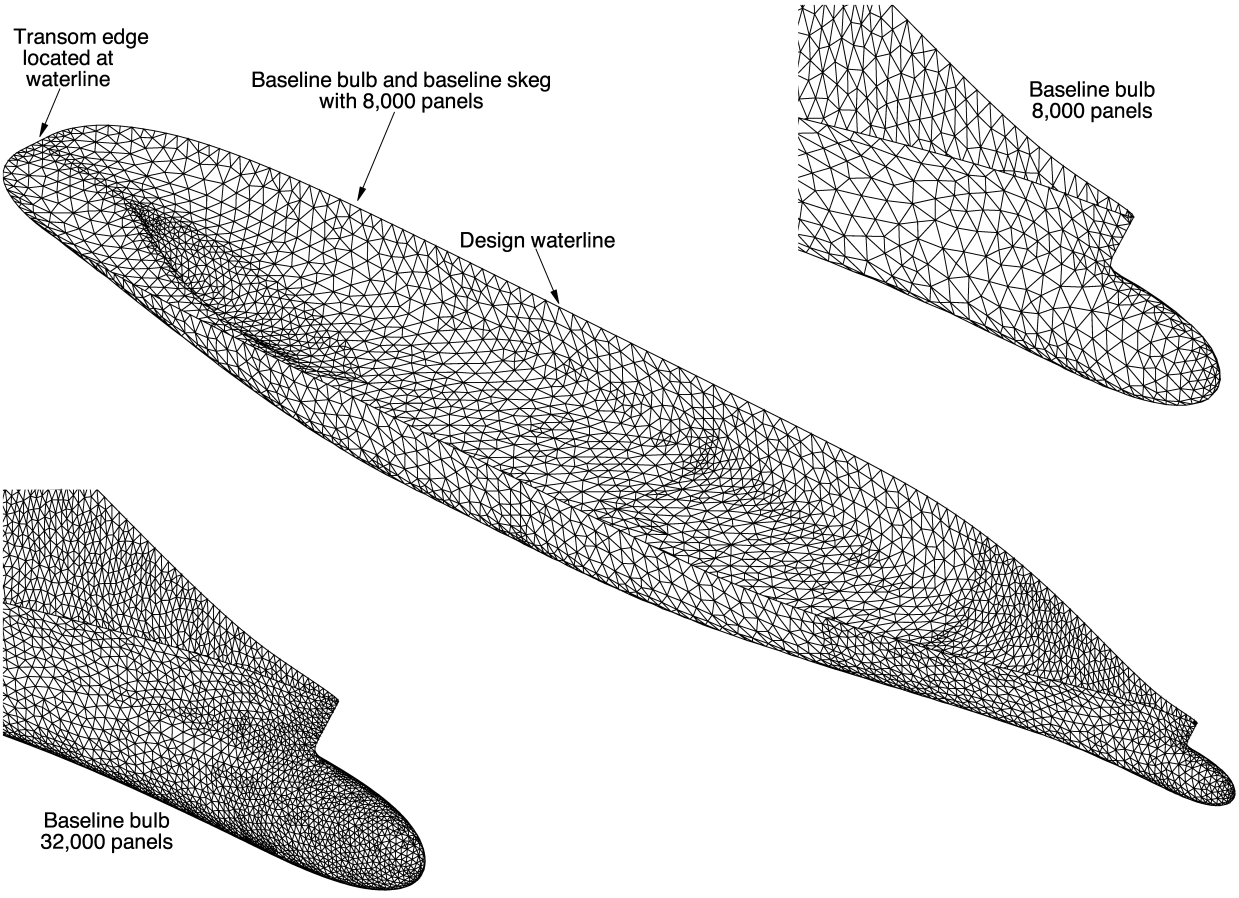

Fig. 1. Baseline hull.

hull-to-hull comparisons. Specifically, the baseline-bulb/baseline-skeg hull is compared to the five hulls

BULB	SKEG	IDENTIFIER
no bulb	baseline	no bulb
nabla 1	baseline	nabla 1
nabla 2	baseline	nabla 2
nabla 3	baseline	nabla 3
producible	baseline	producible

and the baseline-bulb/producible-skeg hull is compared to the hull

BULB	SKEG	IDENTIFIER
nabla 6	producible	nabla 6

The six hull-to-hull comparisons are referred to in the remainder of this paper by the identifiers listed in the tables (no bulb, nabla 1, nabla 2, nabla 3, producible, nabla 6).

3. Experimental drag

The drag D of a ship advancing at constant speed U along a straight path in calm-water is expressed as

$$2D = \rho U^2 S^{\mathrm{A}} C_{\mathrm{T}} = \rho U^2 L_{\mathrm{ref}}^2 \hat{C}_{\mathrm{T}} \tag{1a}$$

where ρ is the water density, S^{A} is the wetted-hull surface area, L_{ref} is a reference length (typically the length of the ship), and C_{T} and $\hat{C}_{\mathrm{T}}$ are nondimensional drag coefficients. We have

$$\hat{C}_{\mathrm{T}} = C_{\mathrm{T}} S^{\mathrm{A}} / L_{\mathrm{ref}}^2 \tag{1b}$$

Models of the eight variant hull forms have been tested in the DTMB tow tank at model-scale speeds corresponding to full-scale speeds in the range of 10–26 knots. The model-scale ratio for the 635 ft Strategic Sealift Ship is $\lambda = 32.495$. The ship models were free to pitch, heave and roll in these resistance tests, but were restrained in surge, sway and yaw. Further information about the resistance tests may be found in Refs. [28,29].

The results of the model tests reported in Refs. [28,29] are summarized in Fig. 4, which depicts the experimental drag coefficient

$$\hat{C}_{\mathrm{T}}^{\mathrm{exp}} = (C_{\mathrm{R}} + C_{\mathrm{F}}) S^{\mathrm{A}} / L_{\mathrm{ref}}^2 \tag{2}$$

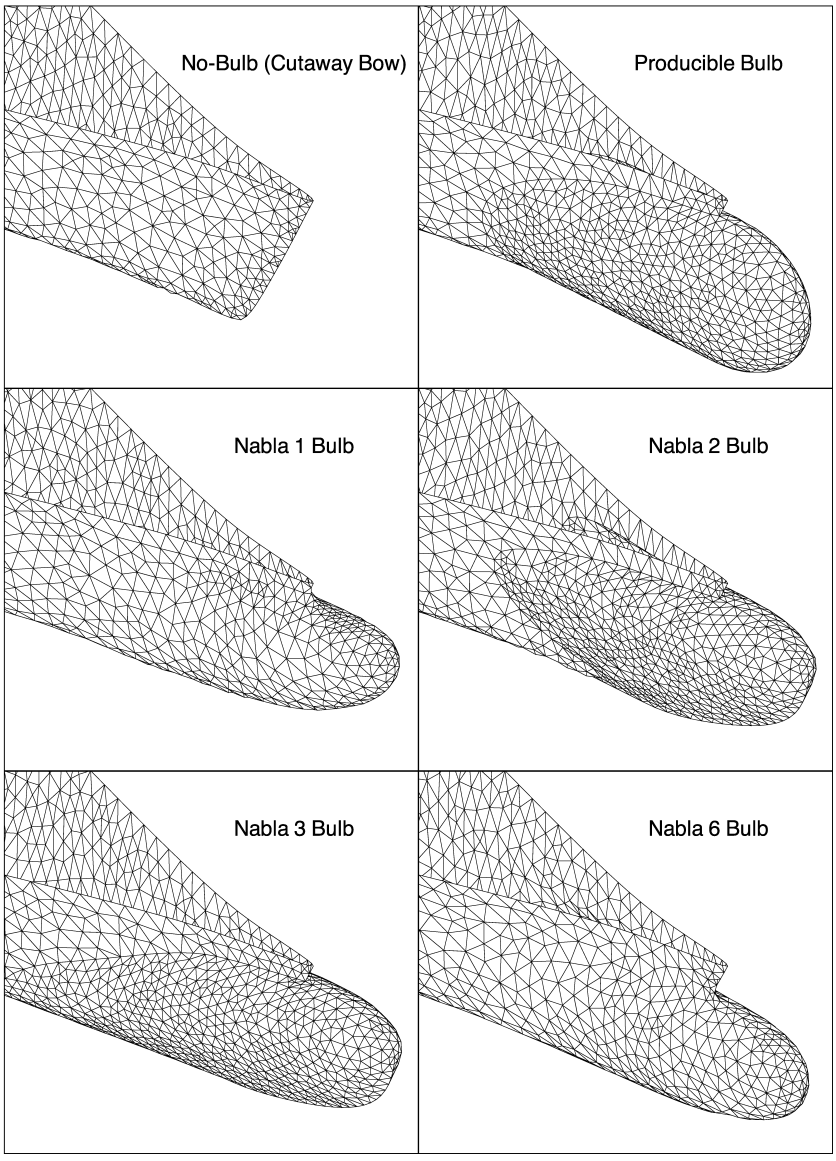

Fig. 2. Forebody variants.

for the eight hull forms as a function of the Froude number $F = U/\sqrt{gL_{\text{ref}}}$ in the range

$$0.16 < F < 0.31$$

The reference length L_{ref} is taken as the length (between perpendiculars) of the ship models, and g stands for the acceleration of gravity. C_{R} in Eq. (2) is the residuary-drag coefficient—reported in Refs. [28,29]—and the friction coefficient C_{F} is given by the ITTC 1957 model-ship correlation line formula

$$C_F = 0.075/[\log_{10}(R_{\text{e}}) - 2]^2 \tag{3}$$

where R_{e} is the Reynolds number of the full-scale ship.

Fig. 4 shows that differences among the drags of the six bulbous-bow models are relatively small, and that the no-bulb model has a significantly larger drag (except at low speed) than the six bulbous-bow models. Thus, Fig. 4 provides experimental confirmation of the well-established advantage of bulbous-bow ships.

4. Theoretical estimation of drag

The experimental drag coefficient $\hat{C}_T^{\text{exp}}$ given by Eq. (2) is compared in this study to the theoretical drag

$$\hat{C}_{\text{T}}^{\text{theory}} = C_{\text{W}} + C_{\text{F}} S^{\text{A}}/L_{\text{ref}}^2 \tag{4}$$

The wave drag coefficient C_{W} is evaluated using the Havelock formula

$$C_{\text{W}} = \frac{2R_{\text{W}}}{\rho U^2 L_{\text{ref}}^2} = \frac{\nu}{\pi}\int_{-\infty}^{\infty} \frac{\mathrm{d}\beta\kappa}{\kappa - \nu}\left[S_{\text{r}}^2 + S_{\text{i}}^2\right] \tag{5a}$$

for the wave drag R_{W} associated with the energy radiated via

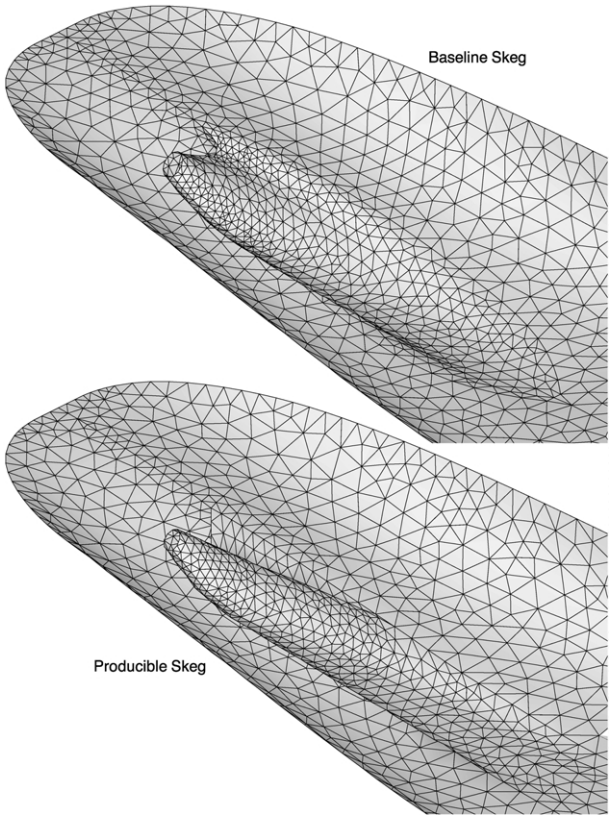

Fig. 3. Skeg variants.

the farfield waves. Here,

$$\nu = \frac{1}{2F^2} \text{ with } F = \frac{U}{\sqrt{gL_{\text{ref}}}} \tag{5b}$$

Furthermore, the wavenumber κ in Eq. (5a) is defined in terms of the Fourier variable β as

$$\kappa(\beta) = \nu + \sqrt{\nu^2 + \beta^2} \tag{5c}$$

S_r and S_i are the real and imaginary parts of the farfield wave spectrum function $S = S(\alpha, \beta)$ where α is defined in terms of the Fourier variable β as

$$\alpha(\beta) = \sqrt{\kappa(\beta)}/F \tag{5d}$$

This relation and expression (5c) for the wavenumber $\kappa = \sqrt{\alpha^2 + \beta^2}$ follow from the dispersion relation $F^2\alpha^2 = \kappa$ for steady ship waves.

The Fourier–Kochin representation of farfield waves given in Refs. [17,18] defines the wave spectrum function S in the Havelock formula (5a) in terms of the disturbance velocity $\vec{u}$ at the mean wetted hull surface. The disturbance velocity $\vec{u}$ at the ship hull can be evaluated using various computational methods. A simple, practical method is the slender-ship approximation given in Ref. [5] and summarized in Ref. [18]. This theory provides a remarkably simple explicit approximation to the velocity $\vec{u}$, and hence to the wave spectrum function S, that is defined directly in terms of the ship speed and the hull geometry.

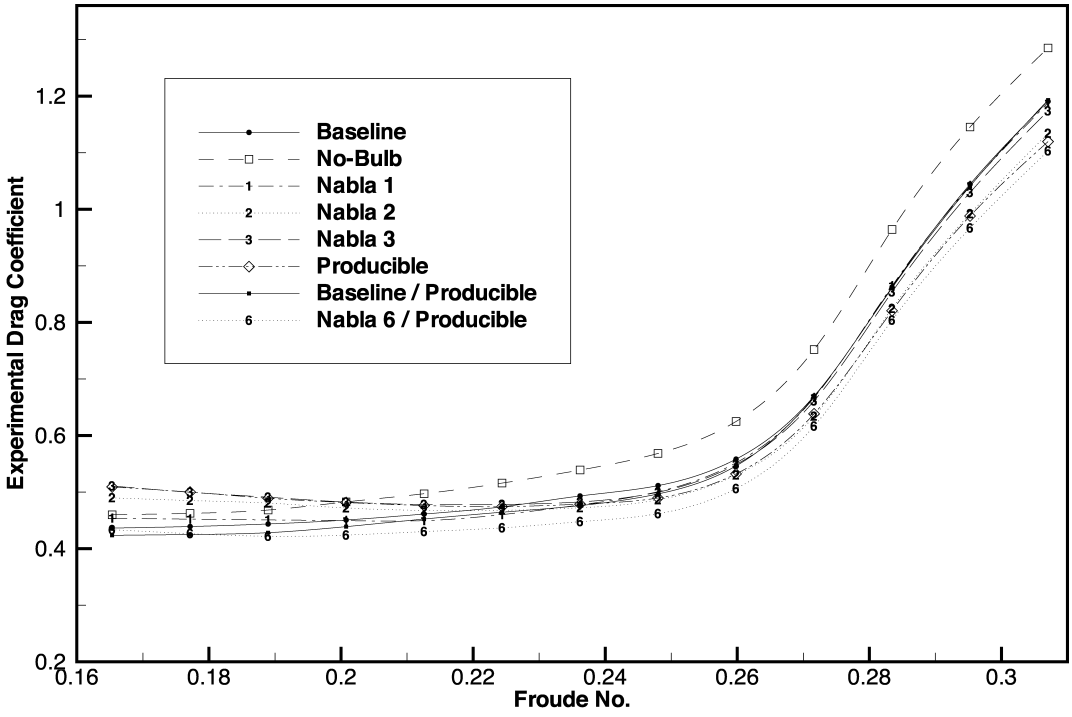

Fig. 4. Measured resistance for a series of eight hulls.

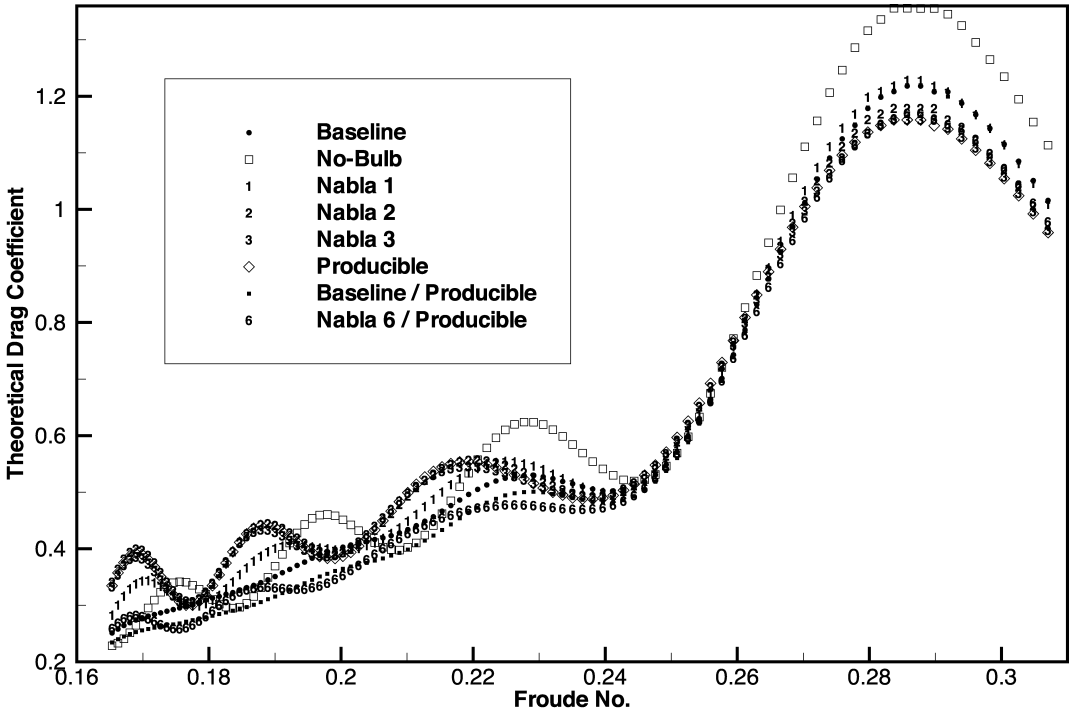

Fig. 5. Computed resistance for a series of eight hulls.

An even simpler approximation to the spectrum function is the zeroth-order slender-ship approximation. This approximation to the farfield wave spectrum function corresponds to the trivial approximation $\vec{u} = 0$ for the nearfield disturbance velocity. The corresponding approximation to the wave spectrum function, given in Refs. [5,18], is

$$S = \int_{\Sigma} n^x \, \mathrm{e}^{\kappa z + \mathrm{i}(\alpha x + \beta y)} \mathrm{d}A + F^2 \int_{\Gamma} (n^x)^2 t^y \, \mathrm{e}^{\mathrm{i}(\alpha x + \beta y)} \mathrm{d}L \quad (6a)$$

Here, dA and dL stand for the differential elements of area and arc length of the mean wetted hull surface Σ and the mean waterline Γ, and

$$(x, y, z) = (X, Y, Z)/L_{\mathrm{ref}} \quad (6b)$$

The x axis is taken along the path of the ship and points toward the ship bow (i.e. the ship advances in the direction of the positive x axis), the z axis is vertical and points upward, and the mean free surface is the plane $z = 0$. Furthermore, n^x and t^y are the x and y components of the unit vectors

$$\vec{n} = (n^x, n^y, n^z) \text{ and } \vec{t} = (t^x, t^y, 0) \quad (6c)$$

normal to the ship hull surface Σ and tangent to the ship waterline Γ; $\vec{n}$ points inside the mean flow domain (i.e. outside the ship) and $\vec{t}$ is oriented clockwise (looking down).

Thus, the wave spectrum function S in the Havelock formula (5a) for the wave drag is defined explicitly in terms of the ship speed and the hull form in the zeroth-order slender-ship approximation (6a). The exceptional simplicity of this approximation to the wave spectrum function (no nearfield-flow calculations are required) renders it ideally suited for hull form optimization.

The zeroth-order slender-ship approximation (6a) may be regarded as a generalization of the classical Michell thin-ship approximation

$$S^{\mathrm{thin}} = \int_{\Sigma} n^x \, \mathrm{e}^{\kappa z + \mathrm{i}\alpha x} \mathrm{d}A \quad (7)$$

Both the thin-ship approximation (7) and the zeroth-order slender-ship approximation (6a) involve simple distributions of elementary wave functions, with strength equal to n^x, over the ship hull. The major difference between the two approximations is that the wave functions are distributed over the ship centerplane $y = 0$ in the thin-ship approximation, while they are distributed on the actual hull surface in the slender-ship approximation. Thus, the shape of a ship hull is mostly accounted for by means of the strength n^x of the wave distribution in the thin-ship approximation, while the slender-ship approximation accounts for the hull shape via both the strength of the wave distribution and the location of the distribution, which is over the actual ship hull instead of over the ship centerplane. Thus, the slender-ship approximation may be expected to provide a more realistic account of hull form than the thin-ship approximation.

Figs. 1–3 show the panelizations used to represent the eight hull forms for the calculation of the wave spectrum function given by Eq. (6). Approximately 8000 unstructured flat triangular panels have been used in these calculations. The theoretical drag $\hat{C}_{\mathrm{T}}^{\mathrm{theory}}$ is depicted in Fig. 5 for the eight hull forms in the range $0.16 < F < 0.31$.

Figs. 4 and 5 show that the theoretical and experimental

drags differ significantly, as might be expected in view of the extreme simplifications embodied in the ITTC friction drag formula and the zeroth-order slender-ship wave drag approximation. However, the question that is under consideration here—and is in fact most relevant for practical applications to hull form design and optimization—is whether a method based on the ITTC friction drag formula and the zeroth-order slender-ship wave drag approximation might be able, despite its extreme simplicity, to rank the drags of a series of hull forms in approximate agreement with experimental measurements.

In fact, the theoretical and experimental results shown in Figs. 4 and 5 may immediately be seen to agree in two notable respects: both Figs. 4 and 5 indicate that (i) differences among the drags of the six bulbous-bow models are relatively small, especially at high speed, and (ii) the no-bulb model has a significantly larger drag than the six bulbous-bow models, except at low speed. Thus, Figs. 4 and 5 provide both experimental and theoretical confirmation of the well-known usefulness of bulbs for reducing drag. The theoretical and experimental results depicted in Figs. 4 and 5 are now analyzed further.

5. Theoretical and experimental comparison of series of hulls

Fig. 6 provides a comparison of both the experimental drag coefficient $\hat{C}_T^{\text{exp}}$ and the theoretical drag coefficient $\hat{C}_T^{\text{theory}}$ for the eight hulls in the series defined in Figs. 1–3. Fig. 6 shows that, although large differences exist among the theoretical and experimental drag coefficients as already noted from Figs. 4 and 5, theoretical and experimental results are in agreement in several notable respects:

(i) Both the theoretical and experimental results shown in the upper left corner of Fig. 6 indicate that the no-bulb hull has a significantly larger drag than the baseline hull over the entire speed range
(ii) Both the theoretical and experimental results in the lower left corner indicate that the modified baseline hull (baseline bulb with producible skeg) has an appreciably larger drag than the nabla 6 hull (nabla 6 bulb with producible skeg), except at low speed
(iii) Both the theoretical and experimental results in the right column show that the baseline bulb yields a larger drag than the producible bulb and the nabla 2 and nabla 3 bulbs in the high-speed range, while the opposite holds in the low-speed range
(iv) The center of the left column also shows agreement between the theoretical and experimental results for the base hull and the nabla 1 hull, which are essentially comparable (although the theory indicates that the nabla 1 hull has a slightly larger drag than the base hull).

Thus, the hull-to-hull comparisons shown in Fig. 6 indicate that, despite their extreme simplicities, the ITTC friction drag formula and the zeroth-order slender-ship wave drag approximation appear to be able to rank the drags of a series of variant hull forms in approximate agreement with experimental measurements.

The procedure used in Fig. 6, based on visual comparison of the (theoretical or experimental) drag curves of alternative hull forms, necessarily involves some degree of subjectivity. A complementary way of comparing the drag curves of two alternative hull forms, say hull A and hull B, consists in defining a ranking coefficient r_B^A as

$$r_{\text{B}}^{\text{A}} = \frac{\sum_{i=1}^{i=n} F_i^3\left(\hat{C}_{\text{T}_i}^{\text{A}} - \hat{C}_{\text{T}_i}^{\text{B}}\right)}{\sum_{i=1}^{i=n} F_i^3\left(\hat{C}_{\text{T}_i}^{\text{A}} + \hat{C}_{\text{T}_i}^{\text{B}}\right)/2} \tag{8}$$

This ranking criterion for comparing hull forms A and B essentially compares the power

$$\rho U^2 L_{\text{ref}}^2 \hat{C}_{\text{T}} U = \rho U^3 L_{\text{ref}}^2 \hat{C}_{\text{T}} \propto F^3 \hat{C}_{\text{T}}$$

required to overcome the drags of hulls A and B for a number of Froude numbers F_i (with $1 \le i \le n$) within a given speed range. The ranking criterion (8) indicates that hull B is better than hull A if $r_{\text{B}}^{\text{A}} > 0$.

The six ranking coefficients

$$r_{\text{no-bulb}}^{\text{base}} \quad r_{\text{nabla 1}}^{\text{base}} \quad r_{\text{nabla 3}}^{\text{base}} \quad r_{\text{nabla 2}}^{\text{base}} \quad r_{\text{prod}}^{\text{base}} \quad r_{\text{nabla 6}}^{\text{base}}$$

determined from both the experimental and theoretical drags depicted in Fig. 6 are now considered. As already noted, approximately 8000 unstructured flat triangular panels were used to represent the eight hulls considered in the calculations reported in Figs. 5 and 6. Calculations using approximately 32,000 panels have also been performed for the purpose of estimating the influence of hull discretization. Figs. 7 and 8 present the experimental and theoretical ranking coefficients for the six hull-to-hull comparisons considered in Fig. 6 in the 'low-speed' and 'high-speed' ranges

$$0.16 < F < 0.24 \qquad 0.24 < F < 0.31$$

Seven ship speeds (equal to 14, 15, 16, 17, 18, 19, and 20 knots) and six speeds (21, 22, 23, 24, 25, and 26 knots) are considered for the low-speed and high-speed ranges, respectively. Thus, n in Eq. (8) is taken equal to 7 and 6 for the low-speed and high-speed ranges, respectively. 'Experiment' in Figs. 7 and 8 refers to the ranking coefficients determined from experimental measurements, and '32k panels' and '8k panels' identify the theoretical ranking coefficients obtained using 32,000 and 8000 panels, respectively. Figs. 7 and 8 show that differences between the theoretical ranking coefficients obtained using 32,000 panels and 8000 panels are negligible for the present purpose.

For the high-speed range, Fig. 8 indicates that theory

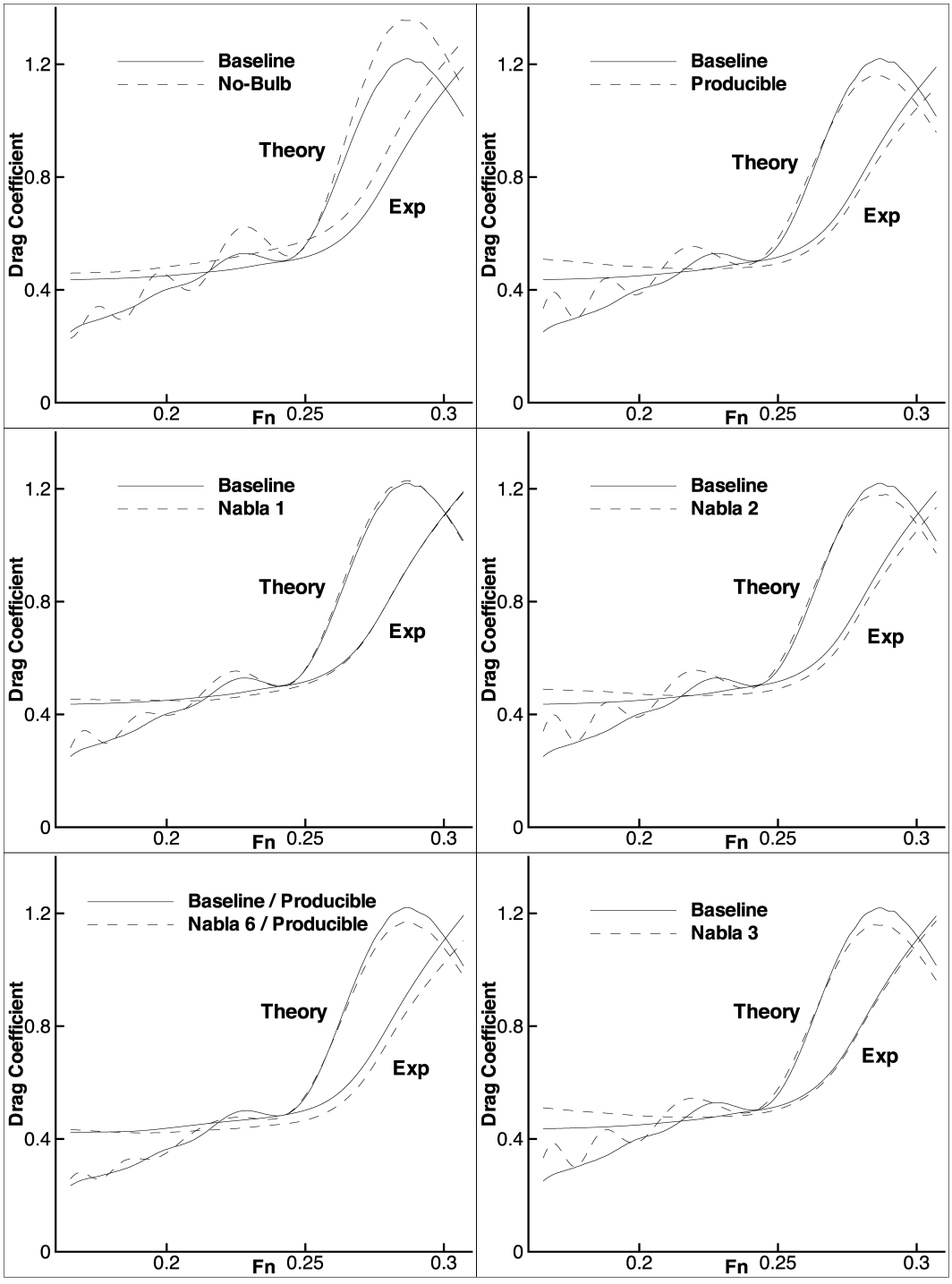

Fig. 6. Comparison of theoretical and experimental drag coefficients for a series of hulls.

and experiments agree in predicting that the no-bulb hull has a significantly larger drag than the baseline hull, and that there is no appreciable difference between the drags of the nabla 1 hull and the baseline hull. Experiments and theory also agree that the nabla 3, nabla 2, producible, and nabla 6 hulls have smaller drags than the baseline hull, although there are appreciable discrepancies between experimental and theoretical results for these 4 cases (especially for the nabla 3 hull). Discrepancies between theory and experiments are relatively larger for the low-speed range considered in Fig. 7, although both theory and experiments agree in predicting that the baseline hull has a smaller drag than the no-bulb, nabla 3, producible, and nabla 2 hulls. Thus, Figs. 7 and 8 show that the theoretical and experimental ranking coefficients are in relatively fair

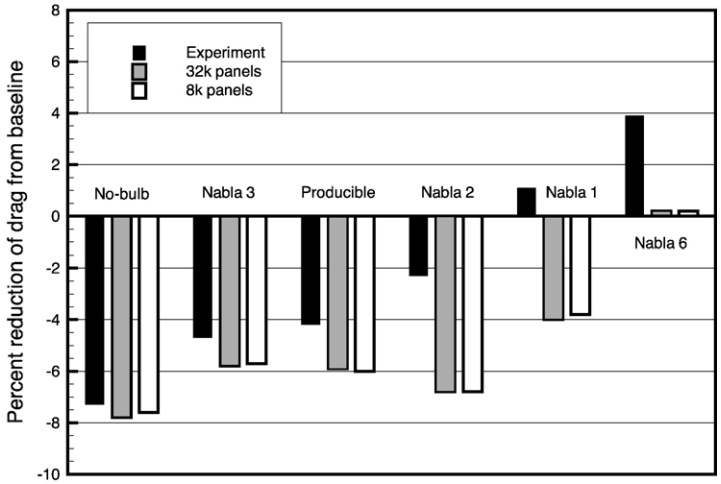

Fig. 7. Experimental and theoretical rankings of drag in the low speed range.

agreement on the whole, considering the extreme simplicity of the theoretical method that has been used to estimate the drag.

6. Hull form optimization example

For purposes of illustration, an optimization procedure is applied to the Wigley hull. This mathematical hull form has parabolic waterlines and framelines, and is defined by

$$y = \pm(1 - 4x^2)(1 - 256z^2)/20 \tag{9a}$$

The volume displacement ∇ of the Wigley hull (9a) is

$$\nabla/L^3 = 1/360 \approx 0.00278 \tag{9b}$$

which yields a 5080 LT (5160 MT) displacement in sea water at a length of 400 ft (122 m). The transverse moment of inertia of the waterplane (moment of inertia about the x axis) I_T is

$$I_T/L^4 = 1/26,250 \approx 0.0000381 \tag{9c}$$

Fig. 9 shows the waterlines (constant-z lines), buttocklines (constant-y lines), and framelines (constant-x lines) of a slightly modified Wigley hull having rounded forefoot and stern. This modified Wigley hull is actually used, in lieu of the classical Wigley hull (9a), as the initial hull in the optimization example considered here. Coordinates in the lines drawing shown in Fig. 9, and further on in Figs. 10–13 for the corresponding optimized hull forms, are nondimensionalized with respect to the length of the initial hull, which is the reference length L_{ref} hereafter. The contour interval in each view is specified by δ.

The nondimensional total-drag coefficient C_T in Eq. (1a) is expressed as

$$C_T = C_W + (1 + k)C_F \tag{10}$$

The wave drag coefficient C_W is evaluated using the zeroth-order slender-ship approximation (6) to the spectrum function S in the Havelock formula (5a). The friction drag coefficient C_F is given by the ITTC 1957 model-ship

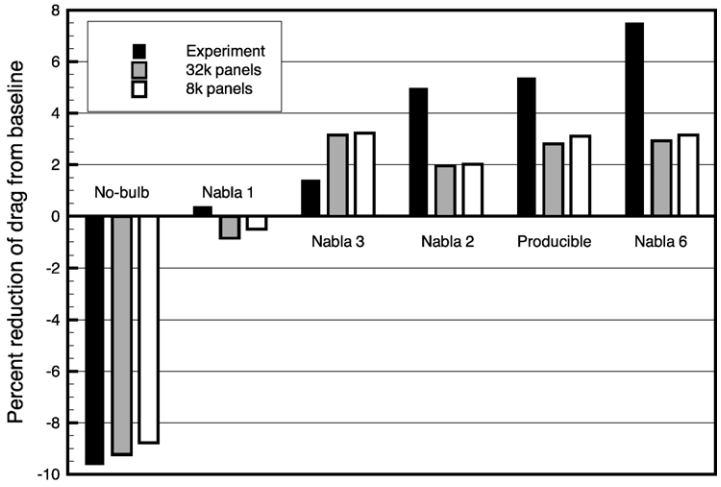

Fig. 8. Experimental and theoretical rankings of drag in the high speed range.

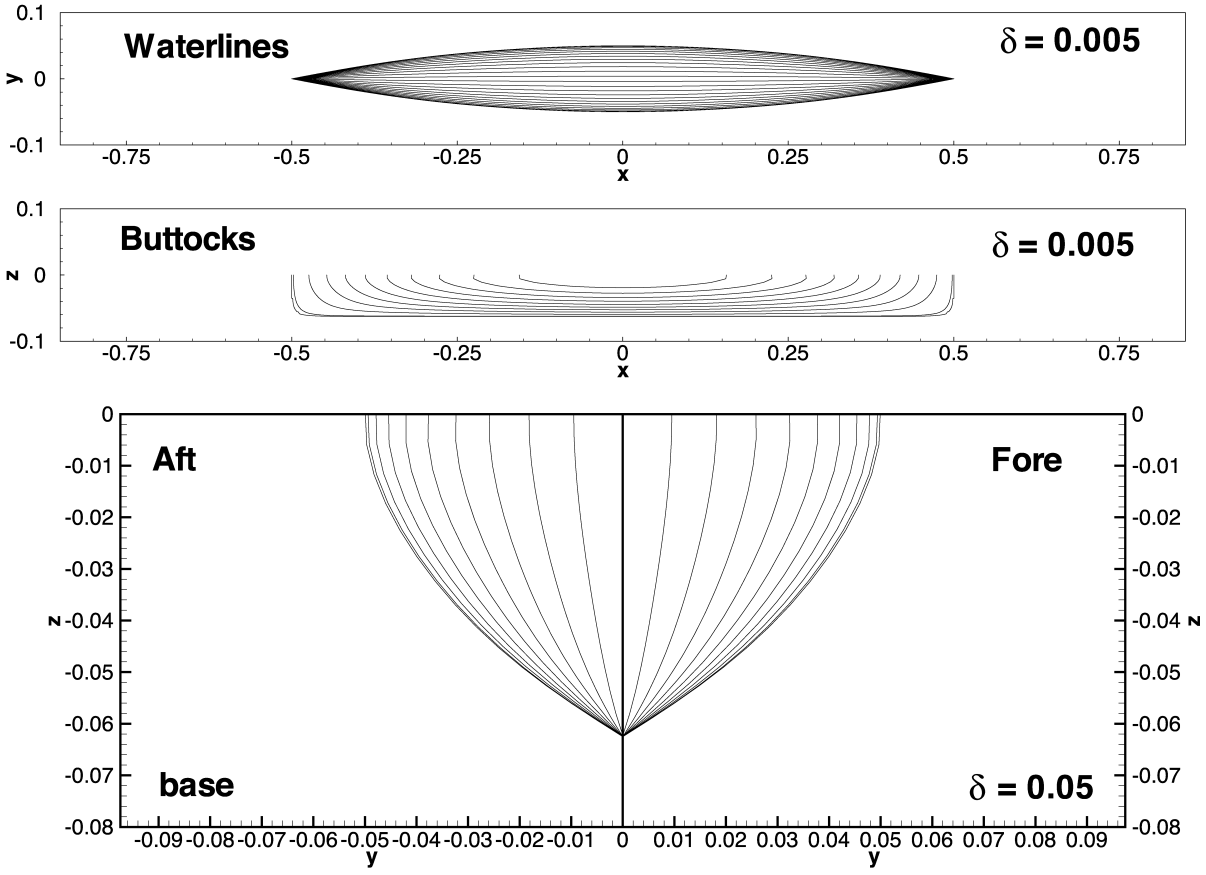

Fig. 9. Lines for the modified Wigley hull taken as initial hull in the optimization.

correlation line formula (3). The form factor k is taken

$$k = 0.6\sqrt{\nabla/L^3} + 9\nabla/L^3 \text{ with} \qquad 0.05 \le k \le 0.40 \qquad (11)$$

where L and ∇ stand for the length and displacement of the ship. Expression (11) is a fit of three data points given in Ref. [30], p. 28.

Optimized hull forms that have the same displacement ∇ and transverse moment I_T as the initial hull and have a minimal total drag $S^A C_T$ are determined. Thus, only two constraints are considered. A real-world optimization problem would obviously involve a number of additional constraints, notably restrictions about principal dimensions (length, draft, beam), and these constraints could be included into the optimization process. However, an idealized (academic) optimization problem involving a minimal number of constraints is purposely considered here to test the capability of the optimization method to generate very different optimized hull forms. Indeed, the optimized hull forms obtained further on (and shown in Figs. 10–13) for three single-speed optimizations and for a three-speed optimization (i.e. four cases in all) are drastically different.

It is important that the wetted-hull surface area S^A be included in the objective function $S^A C_T$ because significant changes in wetted area occur as a result of the optimization procedure. The downhill simplex optimization method, given in Ref. [31] Section 10.4, is used in this study.

As shown in Figs. 10–13, ship hull form optimization may involve large hull form modifications, which must be represented effectively. Thus, a representation of a ship hull surface that is sufficiently flexible and robust to permit large hull form modifications, while involving only a moderate number of unknowns, is an important element of hull form optimization.

In this study, a ship hull is defined as a NURBS (non-uniform rational B-spline [34]) surface. Specifically, a cubic surface with a 5 by 9 control net (5 control points for each of 9 sections) is used to represent a ship hull form, which is assumed to be symmetric about its centerplane $y = 0$. For simplicity, the surface is polynomial (control points are equally weighted) and has uniform knot vectors. The locations of the $5 \times 9 = 45$ control points that define the NURBS surface representing a ship hull are defined in the manner explained in Appendix A.

For the purpose of evaluating the zeroth-order slender-ship approximation (6) to the spectrum function S in the Havelock wave drag formula (5a), a ship hull surface is approximated by a set of flat triangular panels. These panels are defined automatically using the panelization for the initial hull surface, in the manner now explained. A panel vertex is identified by values of the parameters u and v in the

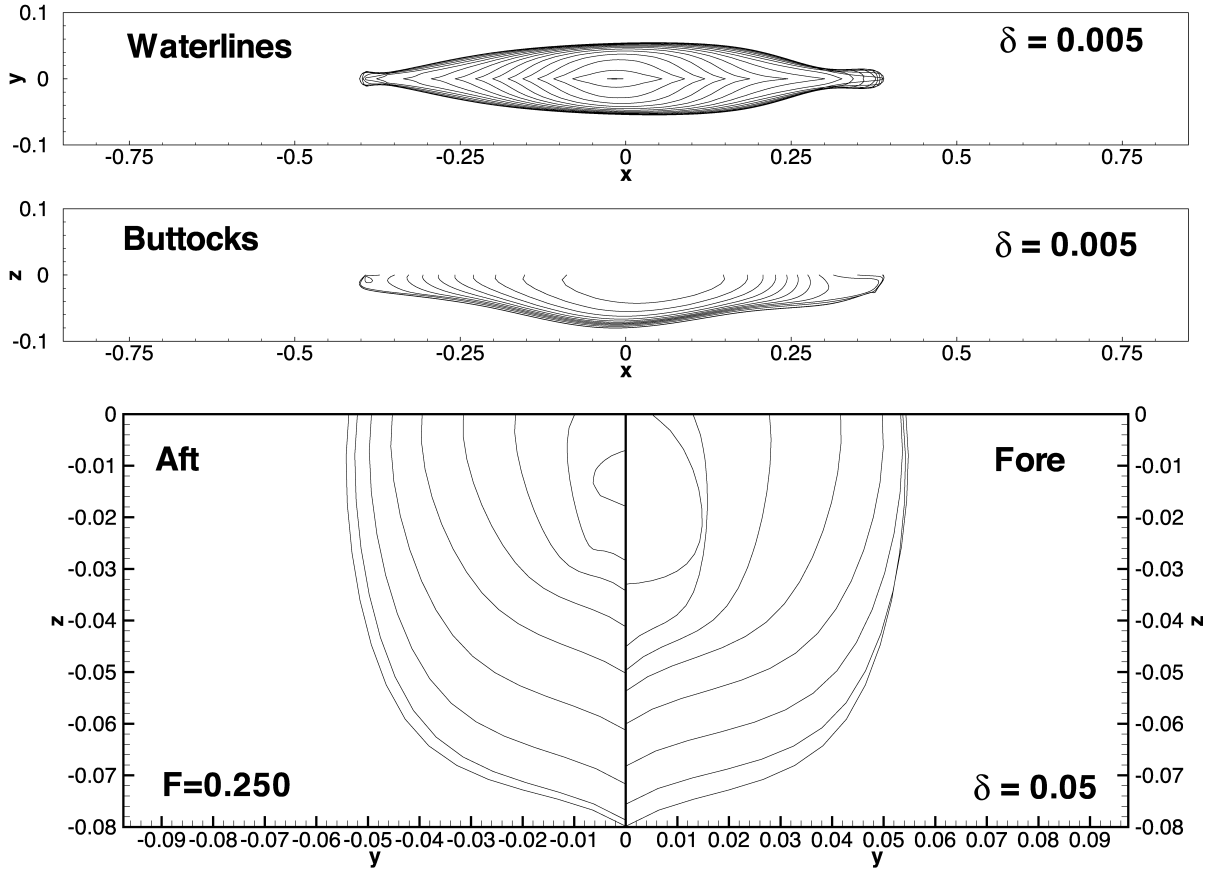

Fig. 10. Lines for hull optimized at $F = 0.250$.

(u, v) parametric representation of the NURBS surface corresponding to the initial surface. The x, y, z coordinates of a panel vertex in the panelization of the hull surfaces that are defined in the course of an optimization are evaluated directly from the values of the parameters u and v attached to the panel vertex in the initial panelization. The volume (displacement) and waterplane-inertia constraints that are considered in the optimization procedure are enforced by iteratively scaling the hull form along the y and (x,z) axes.

In the hull form optimization example reported later, the hull is defined by 61 independent variables (as explained in Appendix A), and is approximated by 11,200 unstructured flat triangular panels. The corresponding computing time is approximately 1.8 s per evaluation of drag for one Froude number on a gigahertz processor. About 12,000–16,000 evaluations of drag are needed until 'complete' convergence. Thus, 18–24 h of computation are required for a hull form optimization over three speeds.

7. Optimized hull forms

Figs. 10–12 depict the waterlines, buttocklines, and framelines of the optimized hull forms obtained by minimizing the drag coefficient $S^{\mathrm{A}}C_{\mathrm{T}}(F)$ for $F = 0.25$, 0.316, and 0.408, respectively. These three Froude numbers correspond to 16.8, 21.2, and 27.4 knots for a 400 ft ship. Fig. 13 depicts the optimized hull form determined by minimizing the sum

$$S^{\mathrm{A}}\left(C_{\mathrm{T}}^{F=0.25} + C_{\mathrm{T}}^{F=0.316} + C_{\mathrm{T}}^{F=0.408}\right) \tag{12}$$

of the drag coefficients at $F = 0.25$, 0.316, and 0.408. Thus, the hull form depicted in Fig. 13 corresponds to a 3-speed optimization, while the hull forms shown in Figs. 10–12 correspond to single-speed optimizations.

Figs. 10–13 show that all three single-speed optimized hulls (most notably the hull optimized at $F = 0.408$) have sizable bow and stern bulbs, while the 3-speed optimized hull has fine ends. The lengths, wetted-hull areas, and displacement to length ratios of the initial hull and the four related optimized hulls are shown in Table 1. The

Table 1
Length, surface area and displacement to length ratio for the initial hull and the four optimized hulls

Hull	L/L_{ref}	$S^{\mathrm{A}}/L_{\mathrm{ref}}^2$	∇/L^3
Initial	1.000	0.144	0.0028
Opt.250	0.793	0.116	0.0056
Opt.316	1.073	0.137	0.0022
Opt.408	1.064	0.143	0.0023
Opt-3F	1.635	0.155	0.0006

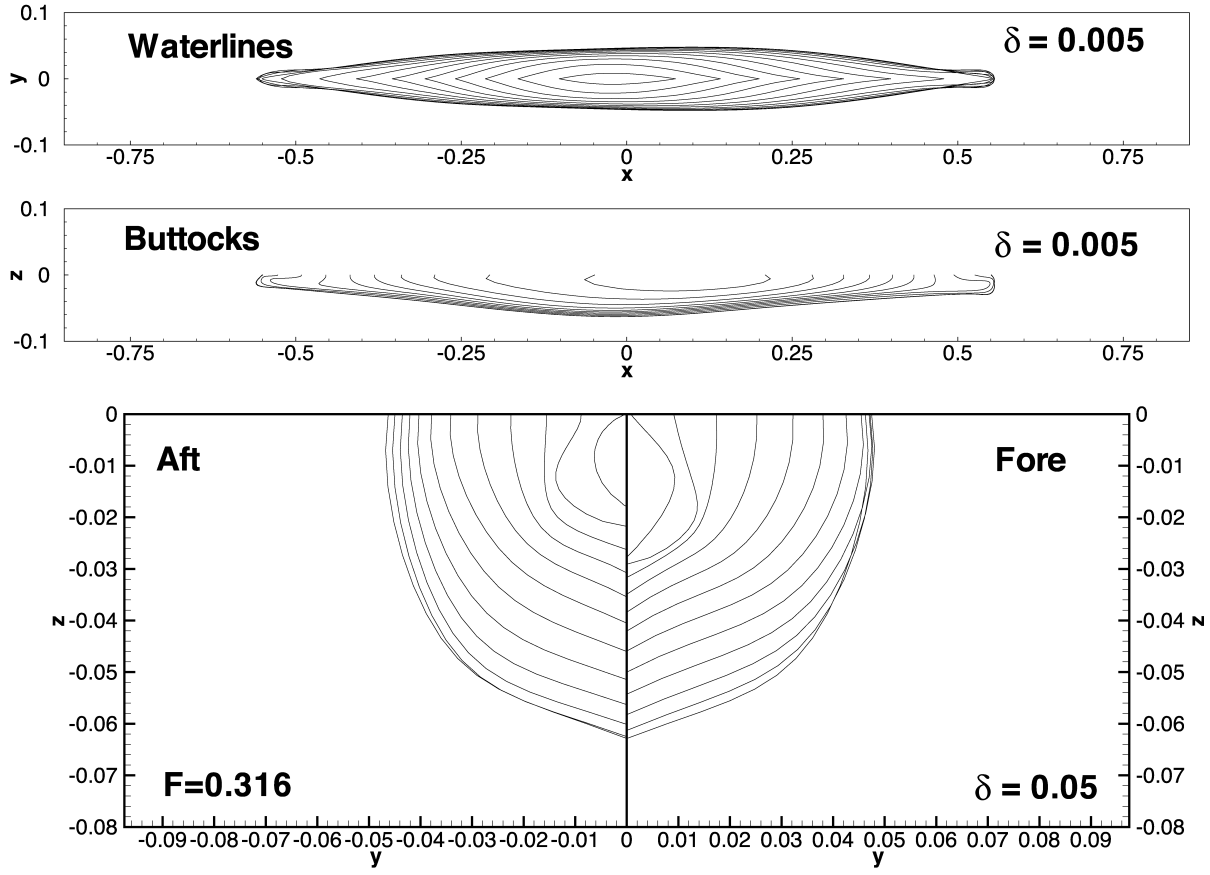

Fig. 11. Lines for hull optimized at $F = 0.316$.

low-speed optimized hull is shorter than the initial hull by more than 20%, while the hulls optimized for $F = 0.316$ and 0.408 are slightly longer than the initial hull, and the 3-speed optimized hull is very much longer. The hull area is reduced (compared to the initial hull) for all three single-speed optimized hulls, most notably for the hull optimized at $F = 0.25$ (for which the friction drag yields the largest contribution to the total drag), and increased slightly for the 3-speed optimized hull.

Fig. 14 depicts the variation of C_W/C_T^0, C_F/C_T^0, and C_T/C_T^0 with respect to the number of evaluations of the objective function in the course of the 3-speed optimization. Here, C_T^0 is the sum of the total-drag coefficients, as in Eq. (12), for the initial hull. Fig 14 shows that the wave drag is reduced first, and quickly becomes quite small compared to the friction drag. The friction drag increases during the early phase of the optimization process. As the optimization process progresses beyond the early phase of rapid reduction in total drag, both the wave drag and the friction drag slowly decrease. During the early phase of the optimization process, the 3-speed optimized hull deforms into a hull having large, deep bulbs at both the bow and the stern. However, as the optimization process continues, these bow and stern bulbs are gradually eliminated, and the hull becomes longer and pointed at the ends as shown in Fig. 13.

Figs. 15 and 16 depict the wave drag coefficient $C_W S^A/L_{ref}^2$ and the total-drag coefficient $C_T S^A/L_{ref}^2$, respectively, of the initial hull, the three single-speed optimized hulls, and the 3-speed optimized hull within the speed range $0.2 \le F \le 0.5$. Fig. 15 shows that the wave drag coefficients C_W for the single-speed optimized hulls are greatly reduced at the Froude numbers for which the hulls are optimized (at $F = 0.25$, 0.316, and 0.408 for the low-speed, intermediate-speed, and high-speed optimized hulls) but increase very rapidly away from the optimization speeds. Thus, single-speed optimization can yield highly-tuned optimized hull forms that perform quite well only in a fairly narrow speed range centered at the optimization speed.

Figs. 15 and 16 also show that the wave drag coefficient C_W and the total-drag coefficient C_T of the 3-speed optimized hull remain small over a broad speed range, in contrast to the drag curves for the three single-speed optimized hulls. Furthermore, the drag of the 3-speed optimized hull is only moderately larger than the drag of the single-speed optimized hulls within the narrow regions where these hulls are optimized. Thus, optimization for a speed range (i.e. multi-speed optimization) appears to be much preferable to optimization for a single speed.

Table 2 lists the values of the wave drag coefficient C_W at

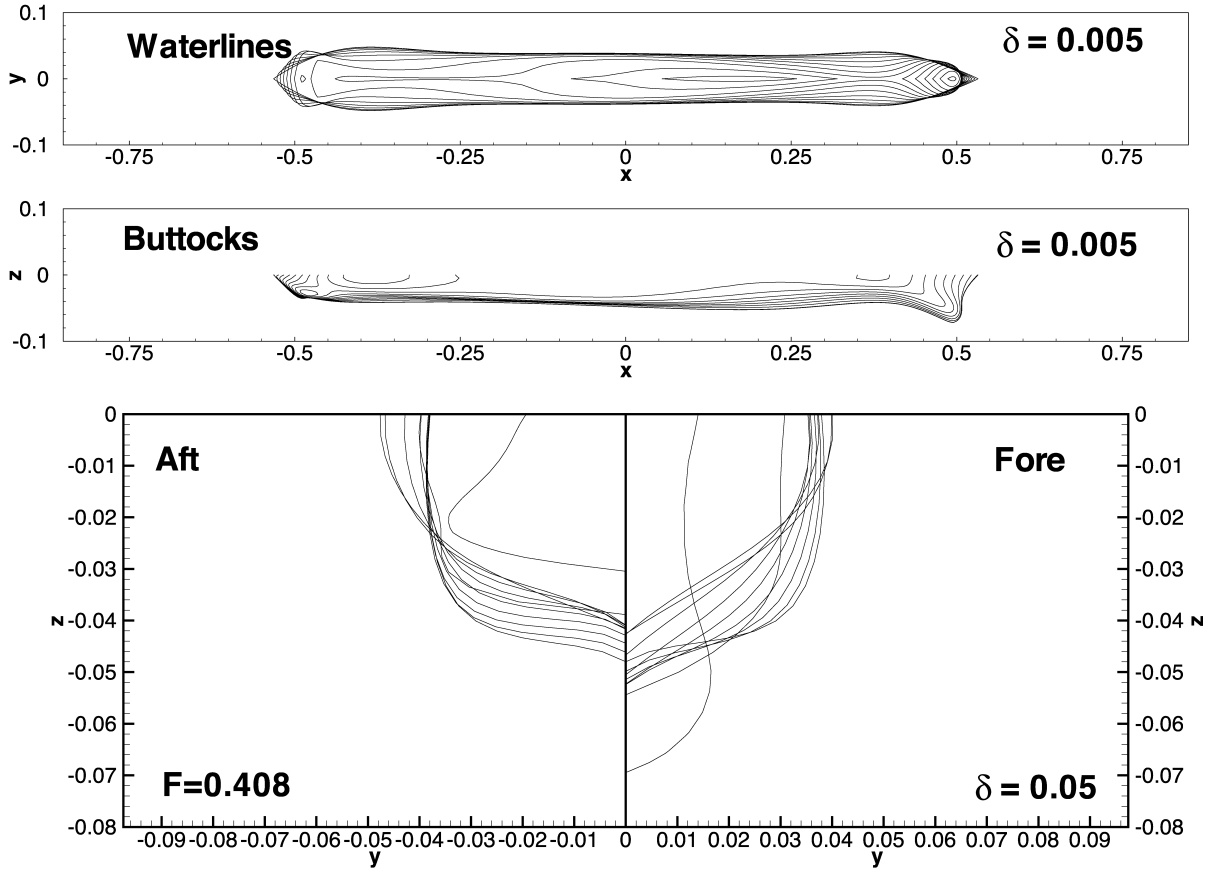

Fig. 12. Lines for hull optimized at $F = 0.408$.

Table 2
Wave drag and friction drag coefficients $10^5\ CS^A/L_{ref}^2$ for the initial hull and the four optimized hulls

Hull	C_W at $F = 0.25$	C_W at $F = 0.316$	C_W at $F = 0.408$	$(1 + k)C_F$
Initial	14.26	22.98	37.36	22.84
Opt.250	0.46			19.06
Opt.316		0.84		21.58
Opt.408			1.78	22.52
Opt-3F	0.22	0.46	2.64	24.42

Table 3
Contribution of wave drag to total drag for the initial hull and the four optimized hulls

Hull	C_W/C_T at $F = 0.25$ (%)	C_W/C_T at $F = 0.316$ (%)	C_W/C_T at $F = 0.408$ (%)
Initial	38	50	62
Opt.250	2	–	–
Opt.316	–	4	–
Opt.408	–	–	7
Opt-3F	1	2	10

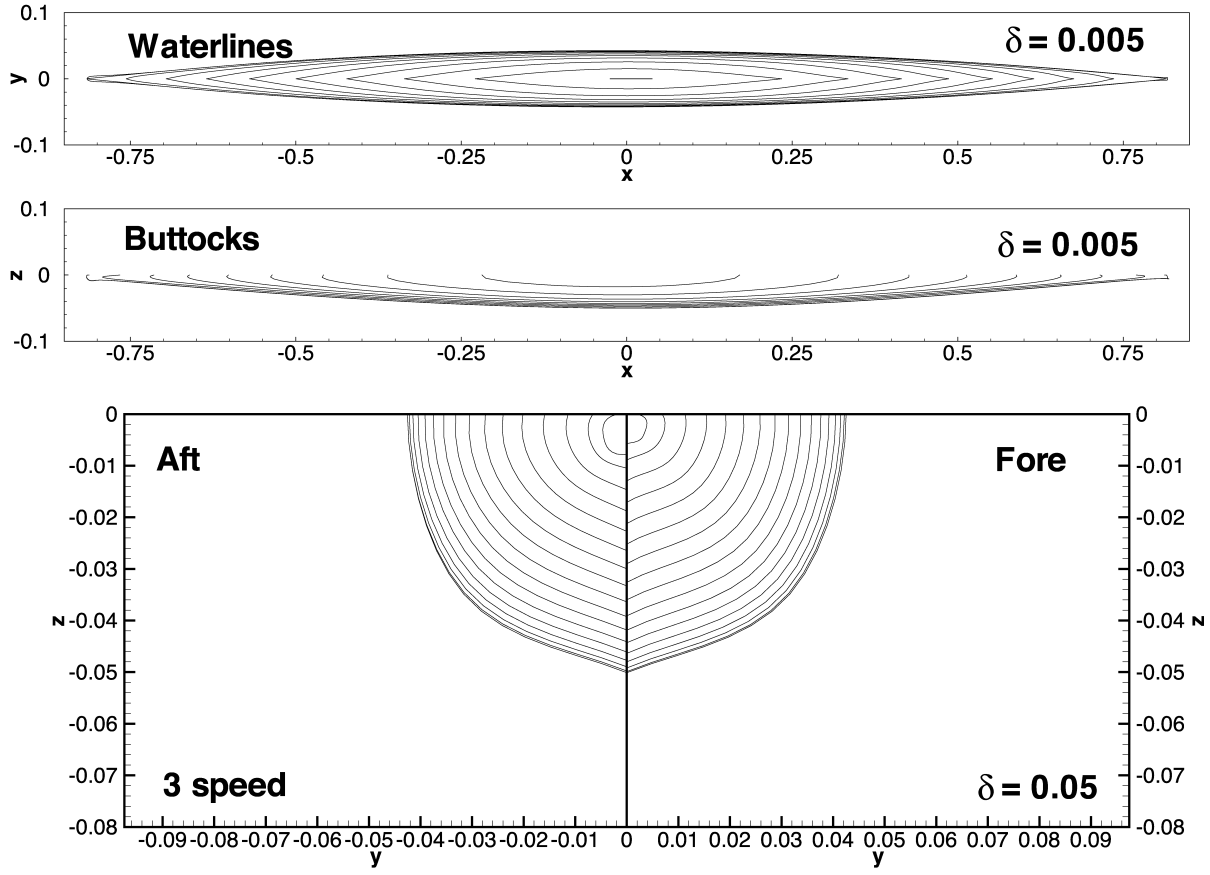

Fig. 13. Lines for hull optimized at $F = 0.25$, 0.316, and 0.408.

$F = 0.25$, 0.316, 0.408, and of the friction drag coefficient $(1 + k)C_F$ for the initial hull, the three single-speed optimized hulls, and the 3-speed optimized hull. In this table, C_W and C_F are multiplied by $10^5\ S^A/L^2_{ref}$.

The ratio C_W/C_T of the wave drag to the total drag is listed in Table 3 for the initial hull, the three single-speed optimized hulls, and the 3-speed optimized hull at $F = 0.25$, 0.316, 0.408. This table shows that the contribution of the wave drag is reduced to near insignificance in the optimized hulls. Indeed, Table 4 shows that the wave drag $C_W S^A/L^2_{ref}$ of the optimized hulls is reduced by 93–98% in comparison to the wave drag of the initial hull.

The corresponding reductions in the friction drag

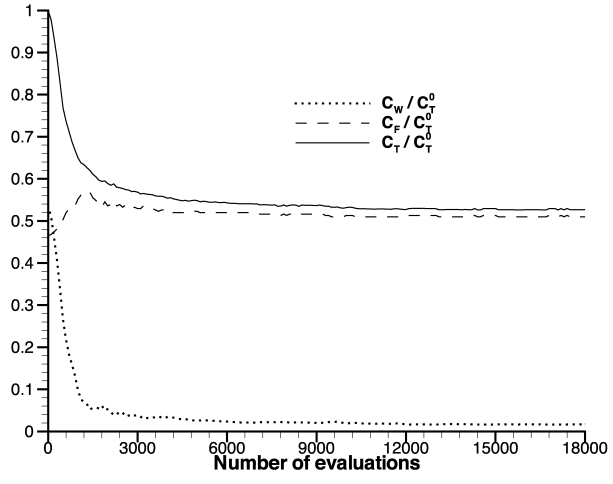

Fig. 14. Variation of drag in course of 3-speed hull form optimization.

Table 4
Reduction in wave drag for the four optimized hulls

Hull	% Reduction in C_W at F		
	0.25 (%)	0.316 (%)	0.408 (%)
Opt.25	97		
Opt.316		96	
Opt.408			95
Opt-3F	98	98	93

Table 5
Reduction in friction and total drags for the three hulls optimized at a single speed

Hull	% Reduction in	
	$(1 + k)C_F$ (%)	C_T (%)
Opt.25	17	47
Opt.316	5	51
Opt.408	1	60

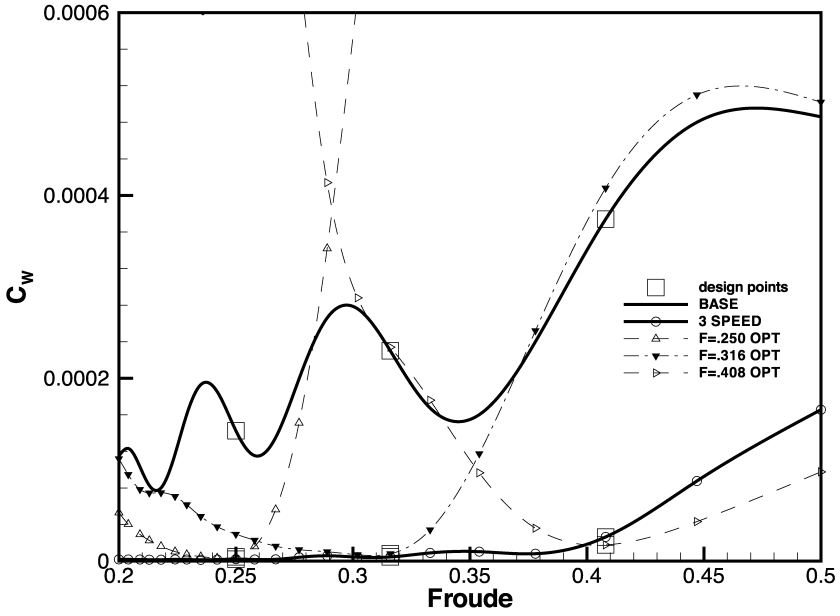

Fig. 15. Computed wave drag for the initial hull and the four optimized hulls.

Table 6
Reduction in friction and total drags for the hull optimized at 3 speeds

Speed	% Reduction in	
	$(1+k)C_F$ (%)	C_T (%)
0.250	−7	34
0.316	−7	46
0.408	−7	55
Mean	−7	47

coefficient $(1+k)C_F$ and the total-drag coefficient C_T are listed in Table 5 for the three single-speed optimized hulls, and in Table 6 for the 3-speed optimized hull. While the friction drag $(1+k)C_F$ of the 3-speed optimized hull is increased by 7%, the total-drag C_T is decreased significantly (although by a lesser amount than for the single-speed optimized hulls). The bottom row in Table 6 lists the mean of the reductions in the values of $(1+k)C_F$ and C_T over the three speeds $F = 0.25, 0.316, 0.408$.

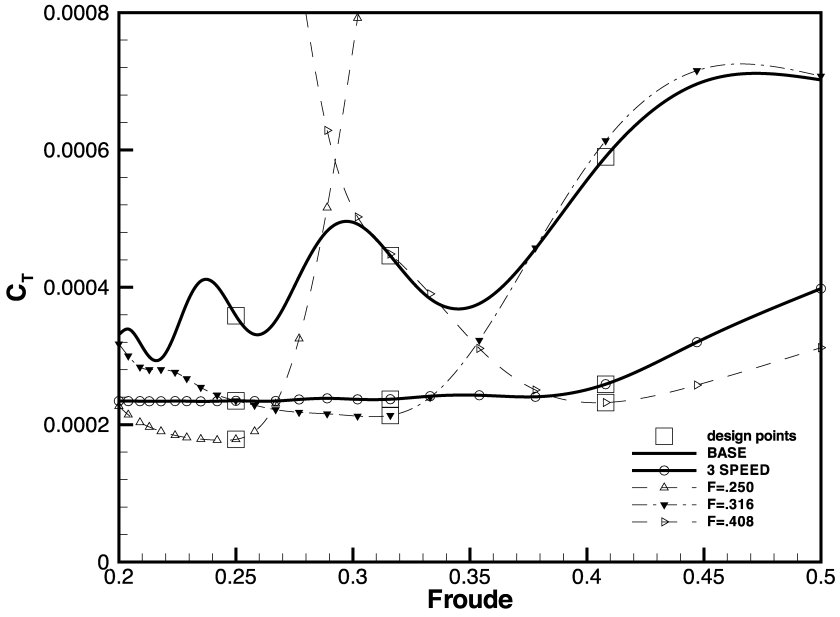

Fig. 16. Computed total drag for the initial hull and the four optimized hulls.

8. Conclusions

The experimental and theoretical drags reported in Figs. 6–8 indicate that the extremely simple CFD tool that has been used to estimate the total drag of a ship, based on the ITTC friction drag formula and the zeroth-order slender-ship wave drag approximation, is able to rank the drags of a series of hull forms roughly in accordance with experimental measurements. The method may therefore be used, with appropriate caution, as a practical hull form optimization tool.

This extremely simple CFD tool has indeed been used to determine ship hull forms that minimize the total (friction + wave) calm-water drag. For purposes of illustration, optimized hull forms that have the same displacement and waterplane transverse moment of inertia as the classical Wigley hull, used as initial hull in the optimization cycle, have been determined for three speeds and for a speed range.

Figs. 15 and 16 show that the wave drag coefficient C_W and the total-drag coefficient C_T of the hull optimized for three speeds remain small over a broad speed range, in contrast to the drag curves of the three hulls optimized for a single speed. Thus, speed-range (multi-point) optimization has been found to be much preferable to single-speed optimization, which yields highly-tuned optimized hull forms that perform well only within a fairly narrow speed range centered at the optimization speed. Furthermore, Figs. 15 and 16 show that the wave and total drags of the 3-speed optimized hull are only moderately larger than the drags of the single-speed optimized hulls within the narrow regions where these hulls are optimized.

Figs. 9–13 show that the wave drag calculation method and the hull form representation that have been used in this study are robust enough to make it possible to explore very large hull form modifications from an initial hull (taken here as the Wigley hull). Tables 3 and 4 show that the wave drag is nearly eliminated as a result of hull form optimization, and Tables 5 and 6 show dramatic reductions in total drag.

The results presented in this study confirm that, despite its extreme simplicity, the zeroth-order slender-ship wave drag approximation can be a useful tool for routine practical applications to hull form design and optimization, as already demonstrated in Refs. [14–16]. It will be interesting to examine the series of eight hull forms and the optimization example considered in this study anew using more refined CFD tools than the extremely simple method that has been employed here. In particular, significant improvements upon the zeroth-order wave drag approximation can be expected from the approximation based on the first-order slender-ship approximation to the nearfield flow and the Fourier–Kochin representation of farfield waves, as explained in Ref. [18]. More refined optimization procedures can also be used, e.g. Ref. [32].

Although optimized hull forms that only take into account calm-water drag have been considered here, it is important to keep in mind that hydrodynamic optimization needs to take into account a number of requirements, including calm-water drag, unsteady motions and loads, and other relevant considerations such as propulsion, cavitation, and wakes. In particular, both motions and calm-water drag should be considered because design and optimization of a ship hull form for calm-water drag without regard to seakeeping characteristics, or minimization of ship motions without regard to drag, can lead to unacceptable hydrodynamic designs. Thus, an integrated approach that simultaneously considers both calm-water drag and motions should be used.

Acknowledgements

The authors wish to thank Don Wyatt, Saad Ragab, and Chi Yang for many stimulating conversations about hull form optimization.

Appendix A. Hull definition

As depicted in Fig. 17, a ship waterline is defined by 9 control points, which evidently are all located in the free-surface plane $z = 0$. The locations of the 2 end control points, which are only permitted to move along the x axis, are defined by 2 unknowns (1 degree of freedom—namely a displacement along the x axis—for each of the 2 end points). The first and last of the 7 interior control points, i.e. the 2 interior control points that are located next to the end points, define the curvature of the waterline at the ship bow and stern within the NURBS representation. Accordingly, the first and last interior control points are presumed

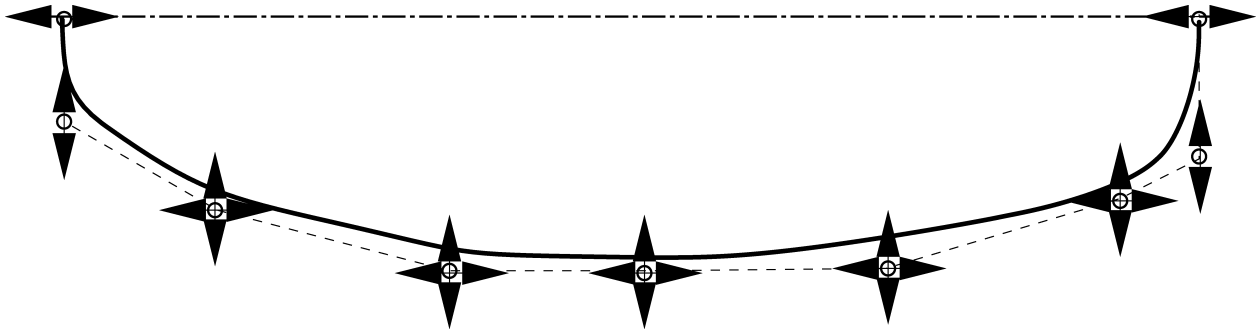

Fig. 17. Plan view of control points defining a ship waterline.

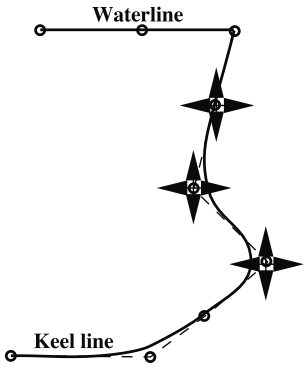

Fig. 18. Profile view of control points defining a ship stem line.

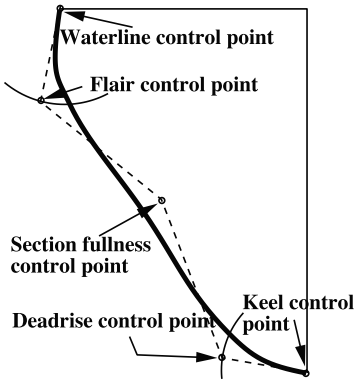

Fig. 19. Body plan view of control points defining an interior station.

to have the same x coordinates as the related end points, and the locations of these 2 interior points are defined by 2 unknowns (1 degree of freedom—a displacement along the y axis—for each of the 2 points). Finally, the locations of each of the 5 remaining interior control points, which are allowed to move within the free-surface plane $z = 0$, are defined by $5 \times 2 = 10$ unknowns (2 degrees of freedom—displacements along the x and y axes—for each of the 5 points). Thus, the locations of the 9 control points that define a waterline involve $2 + 2 + 10 = 14$ unknowns.

A ship keel line is similarly defined by 9 control points, which evidently are all located in the ship centerplane $y = 0$. The locations of each of the 7 interior control points, which are allowed to move within the centerplane $y = 0$, are defined by $7 \times 2 = 14$ unknowns (2 degrees of freedom-displacements along the x and z axes-for each of the 7 interior points). The locations of the 2 end keel line control points are defined in the manner explained further on. Thus, the definition of a keel line involves 14 unknowns.

As already noted, a ship hull form is defined here as a NURBS surface that involves 9 sections. The 2 end sections, i.e. the stem and stern lines, are now considered. As depicted in Fig. 18, the stem line is defined by 5 control points. The locations of each of the 3 interior control points, which can only move within the centerplane $y = 0$, are defined by $3 \times 2 = 6$ unknowns (2 degrees of freedom—displacements along the x and z axes—for each of the 3 interior points). The end point located at the waterline has already been considered. The location of the end point located at the

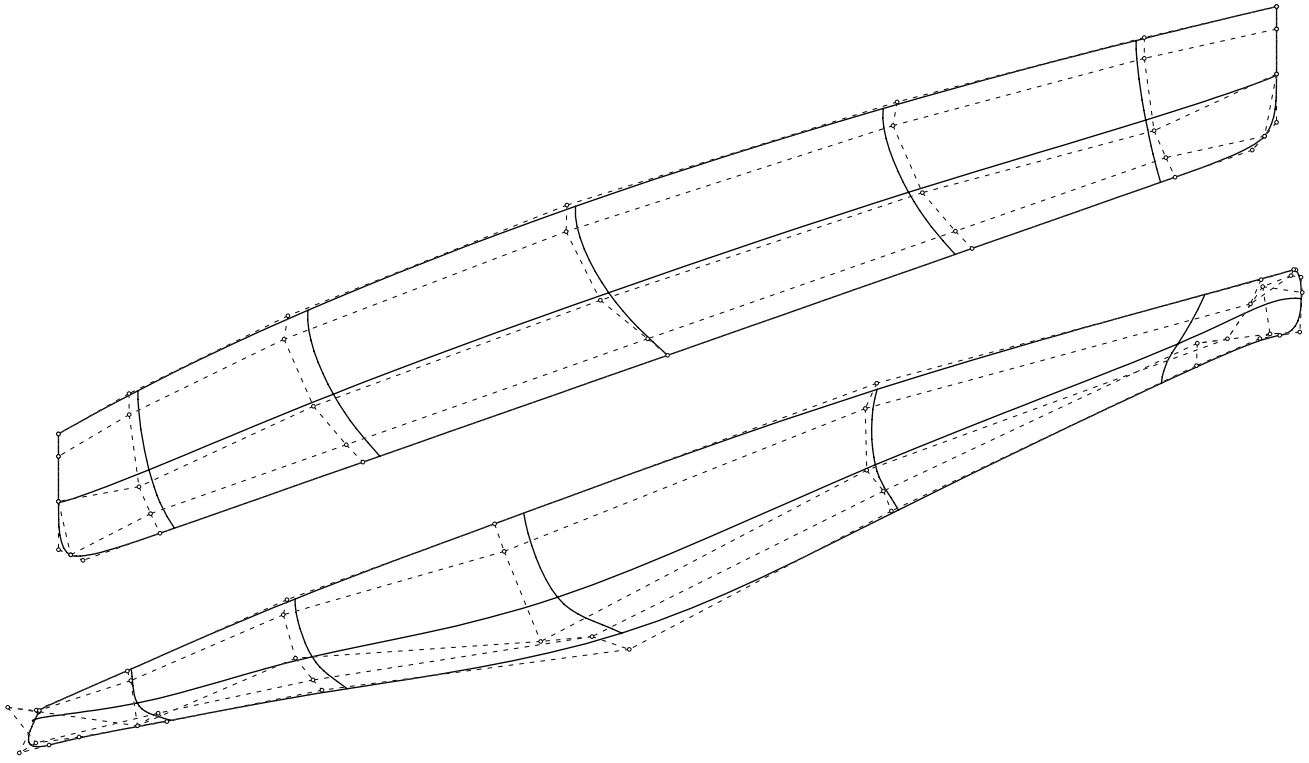

Fig. 20. Control net used to define a ship hull surface.

keel line is defined in the manner explained further on. It follows that the definition of the stem line involves 6 unknowns, and similarly for the stern line. Thus, the definition of the stem and stern lines involve 12 additional unknowns.

The first and last interior sections (sections located next to the stem and stern lines) are now considered. As already noted, these sections define the curvature of the ship hull at the bow and stern within the NURBS representation. Accordingly, the 5 control points that define each of these 2 interior sections are presumed to have the same x coordinates as the related control points on the stem or stern lines. It follows that the definition of the locations of the 3 interior control points (the end points attached to the waterline and the keel line have already been considered) involve 6 additional unknowns (1 degree of freedom—a displacement along the y axis—for each of the 3 interior control points that define the first and last interior sections).

The 5 remaining interior sections are now considered. As depicted in Fig. 19, each of these 5 sections is defined by 5 control points. The 2 end points, attached to the waterline and the keel line, have already been considered. The 3 interior control points define the flair angle, the section fullness, and the deadrise angle, as indicated in Fig. 19. The locations of these 3 interior points is defined by 3 unknowns (1 degree of freedom for each of the 3 interior points) because the x coordinates of the interior points are presumed to vary linearly between the x coordinates of the 2 end points located at the waterline and at the keel line. Thus, the definition of the 5 interior sections now considered involves $5 \times 3 = 15$ unknowns.

All 45 control points have now been considered except for two control points, namely the points that are common to the keel line and either the stem line or the stern line. These points are taken midway between the neighboring points located on the keel line and the stem/stern line. Thus, the definition of these 2 special points does not involve additional unknowns, and the NURBS representation of a ship hull form that is used here involves $14 + 14 + 12 + 6 + 15 = 61$ unknowns. Fig. 20 shows the initial 45-point control net for the initial hull and the corresponding control net for a hull form defined in the course of an optimization.

Several constraints are imposed on the control points to prevent unrealistic hull form deformations. The displacements along the x axis of the interior control points that define the waterline and the keel line are restricted so that each interior point remains between its logical neighbors. The displacements along the z axis of the 3 interior control points that define the stem line and the stern line are similarly restricted to ensure that these interior points are between their logical neighbors.

References

[1] Peri D, Rossetti M, Campana EF. Design optimization of ship hulls via CFD techniques. J Ship Res 2001;45:140–9.

[2] Dejhalla R, Mrsa Z, Vukovic S. Application of genetic algorithm for ship hull form optimization. Il Shipbuild Progr 2001;48:117–33.

[3] Lazauskas L, Tuck EO. Low drag multihulls for sporting, commercial and military applications. FAST'97, Sydney, Australia. 1997.

[4] Day AH, Doctors LJ. The survival of the fittest—evolutionary tools for hydrodynamic design of ship hull form. Royal Inst Nav Arch 2000:142.

[5] Noblesse F. A slender-ship theory of wave resistance. J Ship Res 1983;27:13–33.

[6] Day AH, Doctors LJ. Rapid estimation of near- and far-field wave wake from ships and application to hull form design and optimization. J Ship Res 2001;45:73–84.

[7] Tuck EO, Lazauskas L. Optimum hull spacing of a family of multihulls. Ship Technol Res 1998;45:180–95.

[8] Day AH, Doctors LJ. Resistance optimization of displacement vessels on the basis of principal parameters. J Ship Res 1997;41:249–59.

[9] Birk L, Harries S. Automated optimization—a complementing technique for the hydrodynamic design of ships and offshore structures. COMPIT 2000, Postdam, Germany. 2000.

[10] Doctors LJ, Day AH. Hydrodynamically optimal hull forms for river ferries. Il Symposium on High-Speed Vessels, Royal Institute of Naval Architecture, London, England. 1995.

[11] Hsiung C-C, Shenyan D. Optimal ship forms for minimum total resistance. J Ship Res 1984;28:163–72.

[12] Hsiung CC. Optimal ship forms for minimum wave resistance. J Ship Res 1981;25:95–116.

[13] Hendrix D, Percival S, Noblesse F. Practical hydrodynamic optimization of a monohull. 2001 SNAME Annual Meeting, Orlando, FL. 2001.

[14] Wyatt DC, Chang PA. Development and assessment of a total resistance optimized bow for the AE 36. Marine Technol 1994;31:149–60.

[15] Letcher Jr JS, Marshall JK, Oliver III JC, Salvesen N. Stars & stripes. Sci Am 1987;257:34–40.

[16] Yang C, Noblesse F, Löhner R. Practical hydrodynamic optimization of a trimaran. 2001 SNAME Annual Meeting, Orlando, FL. 2001.

[17] Noblesse F. Velocity representation of free-surface flows and Fourier–Kochin representation of waves. Appl Ocean Res 2001;23:41–52.

[18] Noblesse F. Analytical representation of ship waves. Ship Technol Res 2001;48:23–48.

[19] Campana EF, Peri D, Rossetti M. Ships of the optimum shape by direct numerical optimization. SIAM Conference on Optimization-SIAM OP'99, Atlanta, Georgia. 1999.

[20] Rossetti M, Peri D, Campana EF. Numerical ship hull optimization, Numerical Towing Tank Symposium (NuTTS), Rome, Italy. 1999.

[21] Chou S-K, Huang C-H, Chiang C-C, Huang P-C. An inverse geometry design problem in optimizing the hull surfaces. PRADS 98, The Hague, The Netherlands. 1998.

[22] Söding H. Drastic resistance reductions in catamarans by staggered hulls. FAST'97, Sydney, Australia, 1997. p. 225–30.

[23] Hino T. Shape optimization of practical ship hull forms using Navier–Stokes analysis. 7th Il Conference on Numerical Ship Hydrodynamics, Nantes, France. 1999.

[24] Hino T, Kodama Y, Hirata N. Hydrodynamic shape optimization of ship hull forms using CFD. 3rd Osaka Colloquim Advanced CFD Applications to Ship Flow and Hull Form Design, Osaka Prefecture University and Osaka University, Japan. 1998.

[25] Tahara Y, Himeno Y. An application of computational fluid dynamics to tanker hull form optimization problem. 3rd Osaka Colloquim Advanced CFD Applications to Ship Flow and Hull Form Design, Osaka Prefecture University and Osaka University, Japan. 1998.

[26] Hino T. Fluid-dynamic shape optimization using sensitivity analysis of Navier–Stokes solutions. J Kansai Soc Nav Arch, Japan 1996;226:49–54.

[27] Janson C, Larsson L. A method for the optimization of ship hulls from a resistance point of view. 21st Symposium on Naval Hydrodynamics, Trondheim, Norway. 1996.

[28] Forgach KM. Bare hull resistance experiments for the mid-term sealift ship future technology variant fitted with several different bulbous bows as represented by model 5501. David Taylor Model Basin, NSWCCD, Report CRDKNSWC/HD-0207-04. 1994.

[29] Forgach KM. Resistance and design propeller powering experiments for the mid-term sealift ships represented by models 5501PR and 5502FP. David Taylor Model Basin, NSWCCD, Report CRDKNSWC/HD-0207-08. 1997.

[30] van Manen JD, van Oossanen P. In: Lewis EV, editor. Resistance, principles of naval architecture, vol. 2. Jersey City, NJ: SNAME, 1988.

[31] Press WmH, Teukolsky SA, Vetterling WmT, Flannery BP. Numerical recipes in FORTRAN. 2nd ed. Cambridge: Cambridge University Press, 1992.

[32] Soto O, Löhner R, Yang C. A stabilized pseudo-shell approach for surface parametrization in CFD design problems. Commun Numer Meth 2001:1.

[33] Day AH, Doctors LJ. Minimum-resistance hullforms for high-speed craft. Royal Inst Nav Arch 1996;138:194–210.

[34] Rogers DF. An introduction to NURBS. San Francisco: Morgan Kaufmann, 2001.